IOP Publishing Journal of Physics: Condensed Matter
J. Phys.: Condens. Matter **32** (2020) 244002 (11pp) https://doi.org/10.1088/1361-648X/ab7ad7

Thermoplastic forming of amorphous metals

Benedikt Bochtler[1,2], Oliver Kruse[1] and Ralf Busch[1]

[1] Chair of Metallic Materials, Saarland University, Saarbrücken, Germany
[2] Amorphous Metal Solutions GmbH, Homburg, Germany

E-mail: benedikt.bochtler@uni-saarland.de

Received 23 October 2019, revised 12 February 2020
Accepted for publication 27 February 2020
Published 20 March 2020

Abstract

Amorphous metals display an extraordinary mechanical strength and elasticity and can at the same time be formed like thermoplastic polymers. These properties make them the ideal material for industrial applications where complex parts have to withstand high mechanical loads. In this work, the thermoplastic formability of amorphous metals is evaluated and discussed in connection to their thermophysical properties. Formability is experimentally assessed in thermoplastic deformation experiments with a constant heating rate, and in isothermal experiments. The results are compared to the theoretical formability values calculated from the thermophysical material properties and found to perfectly coincide. The formability of amorphous alloys can be reliably calculated based on a viscosity measurement in the supercooled liquid region. In isothermal experiments, the maximum formability is obtained at the highest temperatures where crystallization can still be avoided.

Keywords: thermoplastic forming, bulk metallic glasses, amorphous metals, formability, supercooled liquid

Supplementary material for this article is available online

(Some figures may appear in colour only in the online journal)

1. Introduction

Among all metallic materials, only amorphous metals can be thermoplastically formed like polymers, providing a unique advantage over other alloys. Additionally, amorphous metals, or bulk metallic glasses (BMGs), display an extraordinary strength in combination with a large elastic limit, making them interesting for industrial applications. The possibilities of thermoplastic forming (TPF) allow for an easy shaping of parts after the production of the amorphous feedstock material, as it becomes moldable above the glass transition temperature. Complex shapes or elaborate surface patterns can be realized in a single processing step [1]. In order to exploit these possibilities, a profound knowledge about the material, its properties, and the perfect processing conditions are crucial.

Soon after the discovery of the first amorphous metals, the possibility to shape them like a thermoplastic in the supercooled liquid (SCL) region was already considered [2]. It was however not before 1978, when Patterson and Jones reported on the hot forming (or TPF) of amorphous metals near the glass transition [3]. In the following years, BMGs with a significantly higher thermal stability were developed, e.g. the Be-containing Zr-based alloys of the Vitreloy family [4], or later the alloys in the Pt–P system [5]. These compositions had a sufficiently high thermal stability to allow for superplastic forming in the SCL region, which was reported for the first time in 2005 by Schroers [6]. In the following years, many more TPF techniques were investigated, mimicking the processes known from thermoplastics.

One of the possible applications for TPF of BMGs is the fabrication of microstructures and micro-electromechanical systems (MEMS) [7–10], or even metallic photonic crystals [11]. Such products are difficult to produce from metallic materials by conventional fabrication techniques, and complex methods based on lithography, electroplating, and molding are in use. BMGs however, can simply be forged by reusable micro-dies, resulting in three-dimensional MEMS

structures, as first demonstrated by Saotome *et al* [12]. A different approach to exploit the formability of BMGs is blow molding. BMGs can be formed by this technique, which is commonly used for example to produce plastic bottles. Shapes that cannot be realized by any other metal processing method can be achieved. The blow molding of BMGs was reported for the first time in 2007 by Schroers *et al* [13]. They succeeded in obtaining a strain of around 400% for the free expansion of a disk during blow molding. Only some years later, they presented a significantly refined process where actual product shapes could be achieved [14], and in 2019 Kim *et al* reported on blow molding of BMGs using an infrared rapid heating technique [15]. In order to exploit the maximum formability during TPF, Johnson *et al* developed a TPF process with ultrafast heating of the sample by a capacitive discharge heating method [16]. Using this technique, they could achieve heating rates of 10^6 K s^{-1}, bypassing the critical heating rate for crystallization and making accessible the complete SCL region, even above the so-called crystallization nose. Later, they further improved their method [17] and included the possibility of shaping by electromagnetic pulsing [18]. In the last years, significant advances were made in the field of TPF of BMGs. TPF was performed on new classes of BMGs, e.g. Fe-based [19, 20] and Ti-based ones [21]; the production of carbon fiber-BMG composites by TPF was reported by Shamlaye *et al* [22], and Monfared *et al* investigated the adhesion between BMGs and the dies during TPF [23].

While the TPF of BMGs offers multiple new forming possibilities, only a limited processing window is available. Processing temperatures and times need to be exactly known and controlled in order to exploit the potential of this technology. The reason for this lies in the metastable nature of the SCL region and hence the limited time till the onset of crystallization. Therefore, a profound understanding of the time-temperature-transformation (TTT) diagrams of each alloy is crucial. The formability of BMGs is strongly temperature dependent, due to the interplay between viscosity and crystallization time.

In the present work, the thermoplastic formability of 12 different BMGs is assessed in a simple deformation experiment with a constant heating rate. Based on these findings, two alloys are selected for further experiments, resulting in time-temperature-deformation (TTD) diagrams. Finally, the thermoplastic formability of BMGs is discussed and related to the thermophysical material properties.

2. Experimental methods

2.1. Sample production

Alloys were synthesized from high purity raw elements with purities ranging from 99.95 wt% to 99.9995 wt%. For alloys containing phosphorus (P), Ni–P and Fe–P prealloys were produced by inductively melting the two raw elements in a silica tube in a high purity argon atmosphere (see reference [24]). Subsequently, the prealloys were fluxed by re-melting them in dehydrated B_2O_3 in a silica tube in order to remove heterogeneous nucleation sites [25]. The raw elements and the prealloys were alloyed by melting quantities according to the desired composition in an arc-melting furnace under a high purity Ti-gettered argon atmosphere. In order to obtain homogeneous master alloys, samples were flipped and remelted at least three times.

The master alloys were cast into rods with a length of 50 mm and a diameter of 3 mm, using an arc melting furnace with a suction casting inset. There, the alloy was melted in a high purity Ti-gettered argon atmosphere on top of a water-cooled copper mold and then sucked into the mold cavity, thus rapidly cooling the melt and forming an amorphous sample.

The amorphous structure of the samples was checked by x-ray diffraction (XRD) with a PANalytical X′Pert Pro diffractometer using Cu K_α-radiation.

2.2. Thermoplastic forming

TPF deformation experiments with a constant heating rate and isothermal ones were conducted to assess the thermoplastic formability of the amorphous alloys. The as-cast rods were cut into cylindrical samples with a diameter of 3 mm and a length of 7 mm and these standardized samples with a volume of 49.5 mm^3 were used for all TPF experiments.

A custom-built TPF machine was used that allows for rapid heating, pressing, and cooling of samples in a high purity Ar-atmosphere. In first approximation, the TPF machine can be described as a pneumatic hot-press within a vacuum chamber. Samples were positioned between two vertical Cu-pistons whose temperature can be precisely controlled. These pistons were brought in contact with the sample, causing a rapid heating due to heat conduction until the sample reached the temperature of the pistons. Typically, heating rates of around 30 K s^{-1} could be reached in the center of the sample. The desired pressing force of 500 N was then also applied by the Cu-pistons. Hence, the two Cu-pistons acted as heating and pressing unit at the same time. After the desired pressing time, the samples were rapidly removed from the heating and pressing stage by an automatic rotation of the sample holder and positioned between two cold Cu-pistons cooled by a thermoelectric cooler. A rapid cooling of the samples was achieved by pressing the cold Cu-pistons against the samples. Typically, cooling rates of around 30 K s^{-1} could be reached.

Deformation experiments with a constant heating rate were used to assess the maximum deformability of an alloy in a single scan. The temperature of the Cu-pistons was adjusted to a temperature 50 K below the glass transition temperature of the sample (T_g − 50 K). After equilibrating, the whole setup (Cu-pistons and sample) was heated with a constant heating rate of 0.333 K s^{-1} up to a temperature at least 10 K above the crystallization temperature of the chosen rate (T_x + 10 K), resulting in a finally crystalline sample. During the experiment, the temperature of the pistons as well as the displacement of the upper piston were recorded (while the lower piston remains static). After each experiment, the sample was cooled to room temperature by removing it from the combined heating and pressing stage and its mean diameter and its exact thickness were measured with a micrometer screw.

In the case of isothermal deformation experiments, the Cu-pistons were set to the desired pressing temperature and

then brought into contact with the samples in order to rapidly heat them. The samples were then pressed at the chosen temperature for different periods of time. After pressing, they were rapidly cooled between the cold Cu-pistons as described above, in order to preserve the obtained microstructure at the end of the pressing time. The obtained results allow to construct a TPF TTD diagram. The main advantage of this experimental procedure over the one with a constant heating rate is that here the amorphous structure of the sample can be preserved, thus maintaining the advantageous properties of the metallic glass. The selected process parameters were evaluated regarding deformation and the conservation of the amorphous structure.

2.3. Calorimetry

Differential scanning calorimetry (DSC) measurements were performed with a power compensated Perkin-Elmer Hyper-DSC8500 calorimeter. For all samples, DSC standard scans with a constant heating rate of $q_h = 0.333$ K s^{-1} were performed. The onset of the glass transition temperature, T_g, as well as the onset of crystallization, T_x, were determined by tangents on the measurement curves.

In order to measure the low-temperature part of the TTT diagram, isothermal DSC crystallization experiments were performed. Samples were heated to different annealing temperatures with a rate of 2 K s^{-1} and held isothermally until the end of the crystallization event. The heat flow during crystallization was then integrated to determine the enthalpy release and the integration results were used to determine the times of the crystallization transformation for each temperature. A further explanation and visualization of the method can be found in reference [26]. Knowledge about this lower part of the crystallization curve is crucial in order to adjust times and temperatures for all further TPF experiments.

2.4. Viscosity measurements

At temperatures around the glass transition, viscosity was measured by three-point beam bending experiments in a Netzsch TMA 402 thermomechanical analyzer. As-cast amorphous rectangular beams were placed on two sharp supporting edges and a load of 0.1 N was applied downwards to the center of the beam using a wedge-shaped fused silica head. The samples were heated to the desired temperature and then held isothermally at least until the end of the relaxation process while the beam deflection rate during relaxation was measured. The corresponding viscosity can be calculated from the beam deflection rate and geometry [27]. A more detailed explanation of the three-point beam bending (3PBB) TMA viscosity measurements can be found in references [28, 29].

3. Results

The results of the thermoplastic deformation experiments upon heating with a constant rate of 0.333 K s^{-1} and a pressing force of 500 N are summarized in table 1. The experiments were performed on 12 different alloy compositions from different alloy families, including Zr-, Cu-, Fe-, Ni-, Pt-, and Au-based alloys.

The values for the glass transition temperature, T_g, and the length of the supercooled liquid (SCL) region, ΔT_x, originate from DSC measurements. ΔT_x is defined as the difference between the onset crystallization temperature upon heating, T_x, and T_g. The liquidus temperatures, T_l are taken from literature. D^* corresponds to the kinetic fragility parameter according to the Vogel–Fulcher–Tammann (VFT) equation, which is typically used to describe the viscosity of a liquid as a function of temperature. The VFT equation can be written as [30]:

$$\eta(T) = \eta_0 \exp\left(\frac{D^* T_0}{T - T_0}\right), \tag{1}$$

where D^* is the kinetic fragility parameter which describes how much the temperature-induced change in viscosity departs from Arrhenius behavior. Kinetically strong liquids with a high value of D^* display a slower change in viscosity with temperature around T_g. T_0 is the VFT-temperature, where viscosity diverges. The pre-exponential factor, η_0, represents the viscosity at infinite temperature. The D^*-values in table 1 are taken from literature if indicated or result from own viscosity measurements. The viscosity values at T_x are the lowest values measured in the TMA viscosity scans. The final sample deformation after the experiment is labeled as φ and is calculated according to the equation: $\varphi = \ln\left(h_1/h_0\right)$ where h_0 is the initial height of the sample and h_1 the deformed height. In the last column, references for original work on the alloy and TMA viscosity measurements are given. The deformation curve during the TPF experiment and the corresponding viscosity scan for the AMZ4 alloy are exemplarily shown in the supplementary information in figure SI 1.

The results in table 1 clearly show a strong correlation between the maximum sample deformation φ and the minimum viscosity at T_x. As the Pt42 alloy has a very low viscosity of 5×10^5 Pa s at T_x, it reaches a deformation of 281%, which corresponds to a final sample thickness of only 0.42 mm for an initially 7 mm high sample. Samples of the Cu-based alloy CuTi for example only reach a maximum deformation of 155% (1.49 mm final sample thickness), and the minimum viscosity at T_x is 6.9×10^8 Pa s, and hence roughly three orders of magnitude higher than in Pt42.

The other material properties listed in the table do not show a direct correlation with deformability. However, when only one property is changed in a system, a direct influence of said property can be observed. For example in the AMZ4 system, the deformation in pure AMZ4 is much larger (190%) than in the industrial grade version AMZ4 Zr$^{(705)}$ (165%). The main difference between the systems is that the SCL region is about 10 K shorter in the industrial grade alloy, and hence a higher viscosity value is detected at T_x, as both alloys show almost the same kinetic fragility (change of viscosity with temperature).

It should be emphasized that especially ΔT_x alone does not correlate with the deformability, even though the length of the SCL region is often considered as the key indicator for the formability. It should further be mentioned, that viscosity at the calorimetric T_g is not always exactly 10^{12} Pa s, e.g. the Pt42 alloy shows a much lower viscosity already at T_g [31].

Table 1. TPF bulk deformation experiments with a constant heating rate. T_g, glass transition temperature; ΔT_x, length of the SCL region; T_l, liquidus temperature; D^*, fragility parameter; η at T_x, viscosity value at T_x; φ, deformation in %, calculated according to $\varphi = \ln\left(h_1/h_0\right)$. The alloys are sorted by their maximum deformation.

Alloy	Composition (at%)	T_g (K)	ΔT_x (K)	T_l (K)	D^*	η at T_x (Pa s)	φ (%)	Reference
Pt42	$Pt_{42.5}Cu_{27}Ni_{9.5}P_{21}$	514	75	874	15.3[a]	5.0×10^5	281	[5, 31]
Au49	$Au_{49}Cu_{26.9}Si_{16.3}Ag_{5.5}Pd_{2.3}$	396	60	644	21.1[a]	1.7×10^7	238	[34, 35]
ZrAg	$Zr_{48}Cu_{36}Al_8Ag_8$	685	96	1143	24.1	6.0×10^7	233	[36]
AMZ3	$Zr_{60.8}Cu_{28.8}Al_{10.4}$	658	81	1180	~25	1.3×10^8	205	[37, 38]
AMZ4	$Zr_{59.3}Cu_{28.8}Al_{10.4}Nb_{1.5}$	663	80	1203	24.8[a]	1.6×10^8	190	[28]
FeMoPCB	$Fe_{67.5}Mo_{7.5}P_{10}C_{10}B_5$	753	80	1338	20.1	1.4×10^8	180	[39]
Ni69	$Ni_{69}Cr_{8.5}Nb_3P_{16.5}B_3$	668	48	1153	14.9[a]	2.0×10^8	167	[31, 40]
AMZ4 $Zr^{(705)}$	$Zr^{(705)}{}_{60.8}Cu_{28.8}Al_{10.4}$	673	71	1196	25.6[a]	2.0×10^8	165	[41, 42]
Vit106a	$Zr_{58.5}Cu_{15.6}Ni_{12.8}Al_{10.3}Nb_{2.8}$	679	75	1140	24.1[a]	5.5×10^8	165	[42–44]
CuTi	$Cu_{47}Ti_{33}Zr_{11}Ni_6Sn_2Si_1$	689	67	1140	~25	6.9×10^8	155	[45, 46]
Vit101 Sn_2	$Cu_{45}Ti_{34}Zr_{11}Ni_8Sn_2$	681	64	1150	25.3[a]	8.0×10^8	143	[42]
iRon	$Fe_{67}Mo_6Ni_{3.5}Cr_{3.5}P_{12}C_{5.5}B_{2.5}$	714	39	1267	21.3[a]	1.3×10^{10}	20	[26]

[a]Value taken from references in the last column.

Similar values were also reported for other BMGs with a relatively low T_g, e.g. for Au-based alloys [32] and Mg-based ones [33]. Hence, the sole knowledge of T_g, T_x, and D^* is insufficient to describe the complete course of viscosity as a function of temperature, as it does not account for these offsets. These topics will be discussed later on.

For the isothermal deformation experiments, only two of the alloys from table 1 were selected, namely AMZ4 and FeMoPCB. These are the two alloys with the best compromise between deformability and industrial applicability, as they show a sufficiently high GFA and do not contain precious metals.

Viscosity of these two alloys was measured by TMA scans and by isothermal measurements in order to derive a VFT fit. Figure 1 displays viscosity as a function of temperature for AMZ4 (a) and FeMoPCB (b). The black squares represent equilibrium viscosity values and are fitted by the VFT equation (dashed line). The resulting fitting parameters are written down in the figure. The red circles represent viscosity as measured by a TMA scan and above the glass transition they coincide well with the VFT fit. On the bottom, a DSC scan with the same heating rate (0.333 K s^{-1}) is shown as a temperature reference. The data for AMZ4 in figure 1(a) is taken from reference [28].

The gray shaded box in figure 1 marks the TPF processing region [28]. The previous experiments showed that deformation for the used samples and under the applied pressing conditions starts at viscosities of around 10^{10} Pa s, which corresponds roughly to the end of the glass transition region. Hence, the TPF processing region is defined by a viscosity below 10^{10} Pa s and down to the minimum value reached before the beginning of crystallization.

Various temperatures within the defined TPF processing region were chosen for isothermal TPF deformation experiments and different samples were pressed for increasing times. Each set of samples pressed at the same temperature was than analyzed by x-ray diffraction in order to determine if the sample remained amorphous. X-ray diffraction patterns of these measurements are exemplarily shown for two temperatures in the supplementary information in figure SI2.

All samples from the isothermal TPF experiments are displayed in an isothermal TTT diagram in figure 2, according to their processing parameters. AMZ4 is shown in figure 2(a) and the crystallization times are taken from reference [28]; FeMoPCB is shown in figure 2(b). Samples that remained amorphous are indicated by green dots and samples that show first indications for crystallization are indicated by red circles. The crystallization times for the 1%, 50%, and 99% transformation according to the DSC measurements are indicated by the black symbols.

For both alloys, the crystallization times from the TTT diagram coincide rather well with the results from the TPF experiments. It must be mentioned that the temperature control in the TPF is by far less accurate than in the DSC and that the temperature distribution throughout the sample is not completely homogeneous as the sample is heated by conduction through the Cu pistons. Hence, small deviations of the TPF results from the TTT diagram have to be expected.

In the case of AMZ4, crystallization in the TPF samples can be detected when roughly the 50% crystallization time of the TTT diagram is passed. For FeMoPCB, first signs of crystallization can be detected at shorter times in relation to the TTT diagram, roughly between the 1% and the 50% transformation time.

The gray shaded areas in figure 2 indicate a change of viscosity of half an order of magnitude, based on the data from the TMA viscosity measurements. The temperatures at which viscosities of 10^8, 5×10^8, 10^9, and 5×10^9 Pa s are expected are indicated by the blunt arrows. Comparing AMZ4 and FeMoPCB, it can be seen that the crystallization times are very similar within the same viscosity region. Hence, both alloys display a similar TPF processing region regarding time and viscosity.

For each sample the deformation during the TPF experiment is calculated according to the equation: $\varphi = \ln\left(h_1/h_0\right)$, where h_0 is the initial height of the sample and h_1 the deformed height after the experiment. From this data, a TTD diagram for the TPF of AMZ4 and FeMoPCB is constructed, as displayed in figure 3.

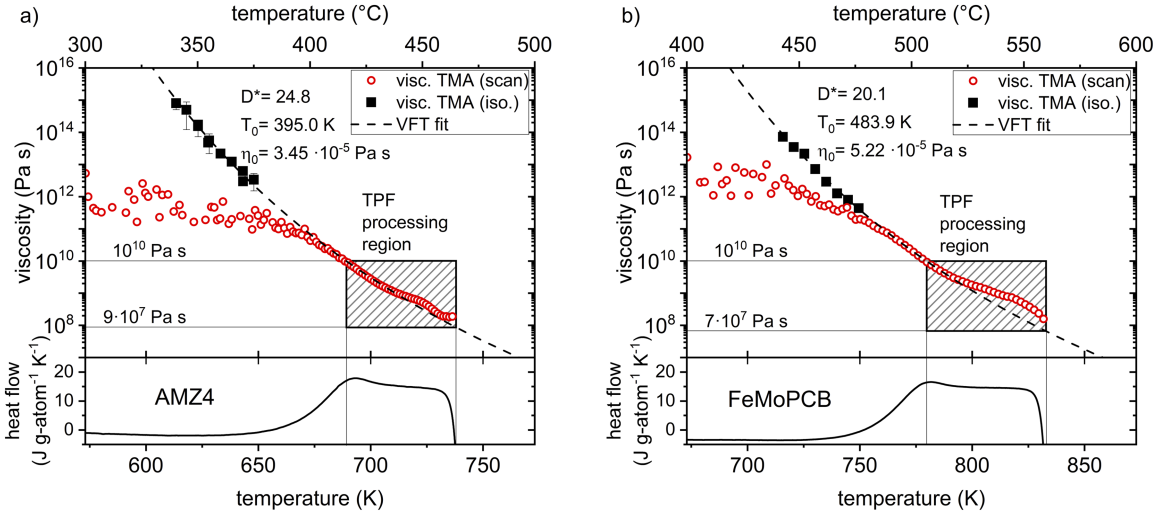

Figure 1. Viscosity as a function of temperature. The black squares represent equilibrium viscosity values as measured in TMA and are fitted by the VFT equation (dashed line). The resulting fitting parameters are written down in the figure. The red circles represent viscosity as measured in a TMA scan and above the glass transition they coincide well with the VFT fit. On the bottom, a DSC scan with the same heating rate (0.333 K s^{-1}) is shown as a temperature reference. The TPF processing region between a viscosity of 10^{10} Pa s and the onset of crystallization is marked by the shaded area. (a) Viscosity of AMZ4, data from [28], and (b) viscosity of FeMoPCB.

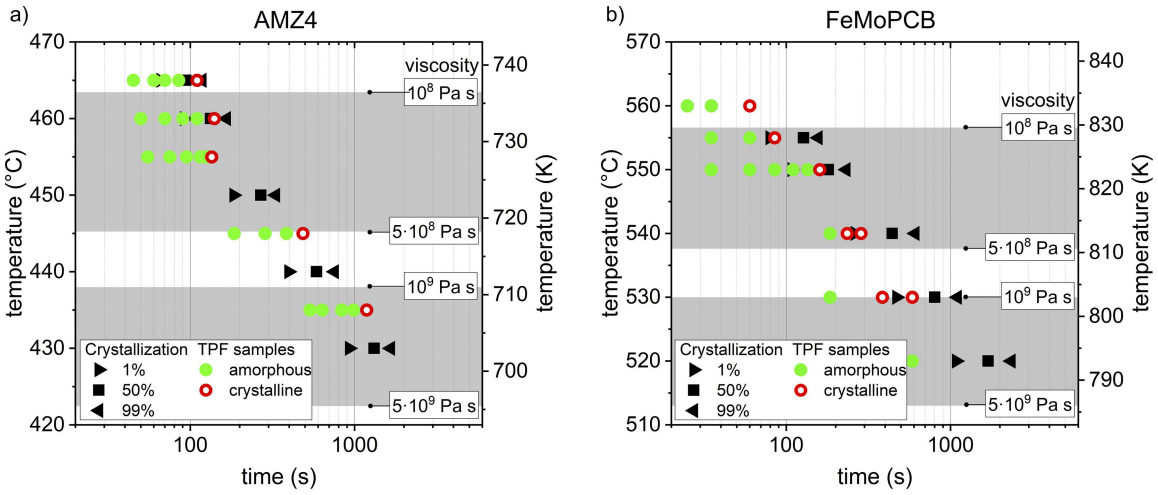

Figure 2. Isothermal TTT diagrams for (a) AMZ4 and (b) FeMoPCB in the TPF temperature range. The black symbols indicate the crystallization transformation in the DSC. All TPF samples that were prepared and analyzed are indicated according to their processing conditions (temperature and time). Samples that stayed amorphous are depicted as green dots and samples that began to crystallize are depicted as red circles. Viscosity values calculated from the VFT fits in figure 1 are given for four temperatures as indicated by the blunt arrows. The gray shaded areas indicate a change of viscosity of half an order of magnitude. (Crystallization times and viscosities for AMZ4 are taken from reference [28]).

The deformation during the isothermal TPF experiments is visualized in a color-filled contour plot, where dark red indicates a deformation above 200% and purple a deformation of 75%. The deformation map is embedded in the TTT diagrams from figure 2 and the prepared samples are indicated by black dots. Crystallization and viscosity values are displayed in the same way as before.

When comparing the two alloys, FeMoPCB displays a larger deformation than AMZ4, with the maximum reaching a value of 215% at 555 °C and 85 s. The maximum value for AMZ4 is 195% at 465 °C and 110 s. In this comparison, the kinetically more fragile alloy, FeMoPCB, shows a larger decrease in viscosity throughout a SCL region of similar length, thus explaining the better formability.

The existence of this ideal processing window at high temperatures also explains why both sample alloys demonstrate a higher deformability in the isothermal experiments than in the ones with a constant heating rate. For a large thermoplastic deformation, it is advantageous to reach the upper limit of the accessible temperature region as fast as possible, in order

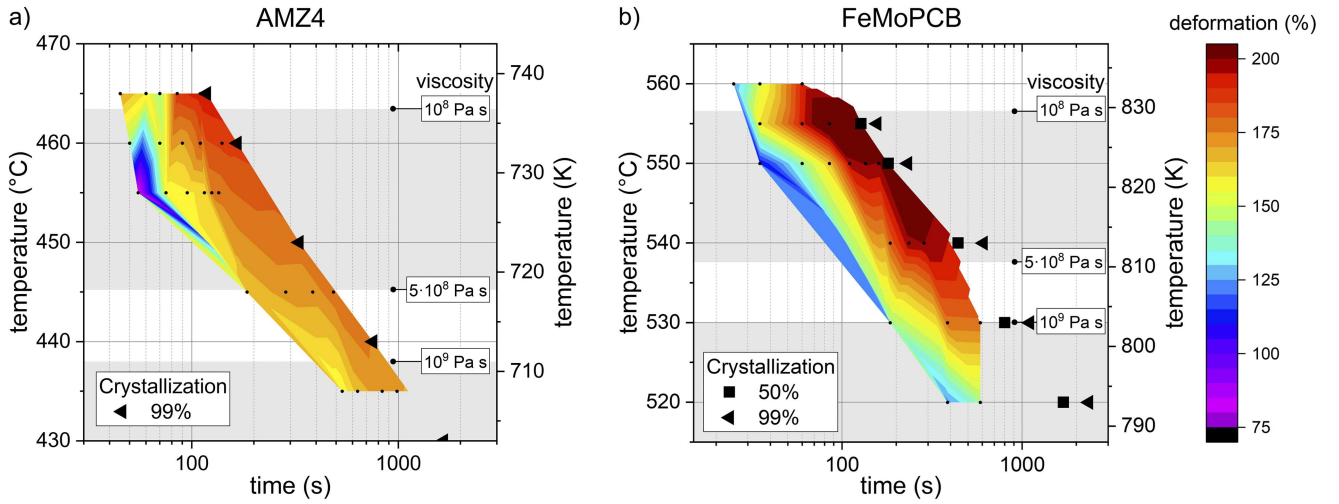

Figure 3. TTD diagrams for the TPF of (a) AMZ4 and (b) FeMoPCB. The deformation during isothermal TPF experiments is visualized in a color-filled contour plot, where dark red indicates a deformation above 200%. The deformation map is embedded in the TTT diagrams from figure 2 and the prepared samples are indicated by black dots. Crystallization and viscosity values are displayed in the same way as before.

to deform the sample at the lowest viscosity for the longest amount of time possible, rather than deforming for longer times at higher viscosities.

4. Discussion

In order to understand the connection between the material properties and their thermoplastic formability, the results of the TPF deformation experiments need to be connected to the thermophysical properties of the alloys. The formability of BMGs in the SCL region was first described by Schroers [47]. In theory, the formability is defined by the maximum strain, ε_{max}, the sample can experience before crystallization. The strain rate, $\dot{\varepsilon}$, for Newtonian behavior can be written as:

$$\dot{\varepsilon} = \sigma/3\eta, \tag{2}$$

where σ is the flow stress and η the temperature dependent viscosity. ε_{max} for isothermal conditions now results from the integration of the strain rate over time, from 0 s to the crystallization time t_c [47]:

$$\varepsilon_{max} = \int_0^{t_c} \dot{\varepsilon}\mathrm{d}t = \int_0^{t_c} \frac{\sigma}{3\eta}\mathrm{d}t = \sigma\frac{t_c}{3\eta} = \sigma F^{iso}. \tag{3}$$

The quantity relating the maximum strain to the applied stress is the isothermal formability F^{iso}:

$$F^{iso}(T) = \frac{t_c(T)}{3\eta(T)}, \tag{4}$$

where both, crystallization time and viscosity, are strongly temperature dependent. In order to calculate the formability parameter for constant heating experiments, F^{scan}, equations (3) and (4) can be adapted [47]:

$$F^{scan}(\dot{T}) = \frac{1}{3\dot{T}}\int_{T_g(\dot{T})}^{T_x(\dot{T})} \frac{1}{\eta(T)}\mathrm{d}T = \frac{1}{3\dot{T}}\int_{T_g(\dot{T})}^{T_x(\dot{T})} \frac{1}{\eta_0}\exp\left(\frac{-D^*T_0}{T-T_0}\right)\mathrm{d}T, \tag{5}$$

where $\dot{T}$ is the applied heating rate of the scan and T_g and T_x are the heating rate dependent glass transition and crystallization temperature, respectively. The temperature dependent viscosity $\eta(T)$ can be expressed in terms of the VFT equation (equation (1)). The formability during a scan strongly depends on the heating rate, mainly through the influence of the heating rate on the crystallization temperature. In this work however, a constant heating rate of 0.333 K s^{-1} was used for all experiments.

In his original work on the formability of BMGs in the SCL region upon heating with a constant rate, Schroers derived several quantities that correlate with the experimentally observed deformation [47]. The best correlation was found for the so-called S parameter, which is defined as $S = \Delta T_x/(T_l - T_g)$, and a good correlation was also observed for $\Delta T_x/T_g$. These quantities are calculated as well for our deformation experiments with a constant heating rate and are depicted over the experimental deformation in % in figure 4 (compare to table 1 for the experimental results). The goal of the experiments in this work is to assess if the reported correlations are universal, and hence hold true for a different experimental setup and different alloys.

Figure 4(a) shows a rather good correlation for $\Delta T_x/T_g$ with the deformation, where the coefficient of determination for a linear fit is $R^2 = 0.82$. While ΔT_x itself does not correlate with the deformation, the normalization to T_g basically scales the length of the SCL region to the intrinsic softening temperature of the system and by this makes them comparable. The correlation found for S, as shown in figure 4(b) is slightly worse, with $R^2 = 0.72$. The material properties needed to calculate

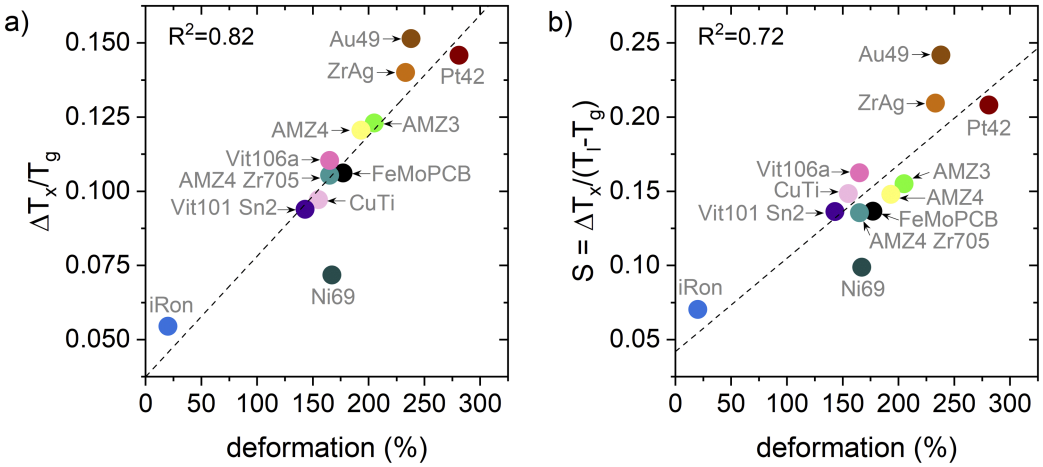

Figure 4. Correlations obtained from the TPF experiments with a constant heating rate (table 1). The dashed lines represent linear fits to the datapoints. (a) Correlation between $\Delta T_x/T_g$ and the experimental thermoplastic deformation in %. (b) Correlation between $S = \Delta T_x/(T_l - T_g)$ and the deformation.

these two predictive quantities can be easily obtained from a DTA measurement. Hence, a quick first prediction of the general formability of a BMG can be made from a single DTA scan.

While the correlation of $\Delta T_x/T_g$ and S with the deformation is reasonable, some outliers are still observed (e.g. Ni69), making it desirable to define a quantity with a better correlation that still is somewhat easy to measure. A single TMA viscosity scan does not require more experimental efforts than a DTA measurement. Such a viscosity measurement results in a dataset that easily allows to obtain the minimum viscosity of the system right before the onset of crystallization at T_x, as noted in table 1. As viscosity in metallic liquids generally decreases with increasing temperature, the viscosity value at T_x is the lowest value that can be reached upon heating before the onset of crystallization causes a rapid increase in viscosity, when the crystalline solid is formed. Consequently, this viscosity value quantifies the maximum flowability of the material during the TPF process and was therefore chooses as evaluation parameter. The correlation of $\eta(T_x)$ with the deformation is displayed in figure 5(a). While not a linear correlation is observed on this logarithmic viscosity scale, no more outliers from the general trend are found. The gray dotted line corresponds to a quadratic fit that is only intended to guide the eye. Hence, a single viscosity measurement allows for a good prediction of the achievable thermoplastic deformation.

Finally, also the theoretical formability parameter for a temperature scan, F^{scan}, is calculated for all investigated alloys, according to equation (5). For each alloy, the inverse of the VFT equation was plotted and numerically integrated from T_g to T_x, resulting in the displayed values. A linear fit to the datapoints shows a very good correlation between F^{scan} and the deformation with a coefficient of determination of $R^2 = 0.94$. This stunning correlation emphasizes the validity of the theoretical formability concept. The correlation between formability and deformation in the original work of Schroers was not as strong as in our work. However, there, viscosity data for the sample alloys was obtained from different literature sources, while in our work all viscosity measurements were performed with the same experimental setup in our group (including the data from cited sources). This emphasizes the necessity for careful and consistent measurements under defined and constant conditions.

While the formability F^{scan} in this case was calculated from VFT fits that can only reliably be obtained from labor-intensive isothermal equilibrium viscosity measurements, the viscosity information for the relevant temperature interval contained in the VFT fits can also be extracted from a single TMA 3PBB viscosity scan. In this case, the course of the viscosity scan can be used for a VFT fit of the temperature region between T_g and T_x without a significant deviation from the VFT fit based on the isothermal measurements. The resulting calculation of F^{scan} according to equation (5) yields very similar values, not challenging the found correlation. Hence, a single TMA viscosity scan can be sufficient to assess the formability F^{scan} of a BMG. However, it should be mentioned that a TMA scan with an excellent data quality is necessary, where especially at higher temperatures, approaching T_x, no measurement artifacts e.g. due to the TMA deflection limit are observed.

The isothermal formability, F^{iso}, corresponding to the TTD diagrams from figure 3 is calculated according to equation (4). The temperature-dependent values of F^{iso} for AMZ4, FeMoPCB and Pt42 are displayed in figure 6 as symbols with connecting lines. Formability is shown over temperature scaled to T_g. The data for AMZ4 (black) and FeMoPCB (red) results from the TTT and viscosity measurements from this work and the Pt42 data is calculated from our previous work [48] and serves as a reference. Note that the formability axis has a break between the Pt42 and FeMoPCB data.

For AMZ4 and FeMoPCB, next to each formability datapoint, the experimentally obtained TPF deformation from the isothermal experiments is noted in % (compare to the TTD diagrams in figure 3). It can be seen, that the isothermal formability values for both alloys follow the trends found in the deformation experiments. In total, FeMoPCB displays a higher formability than AMZ4. For both alloys, a deformation of

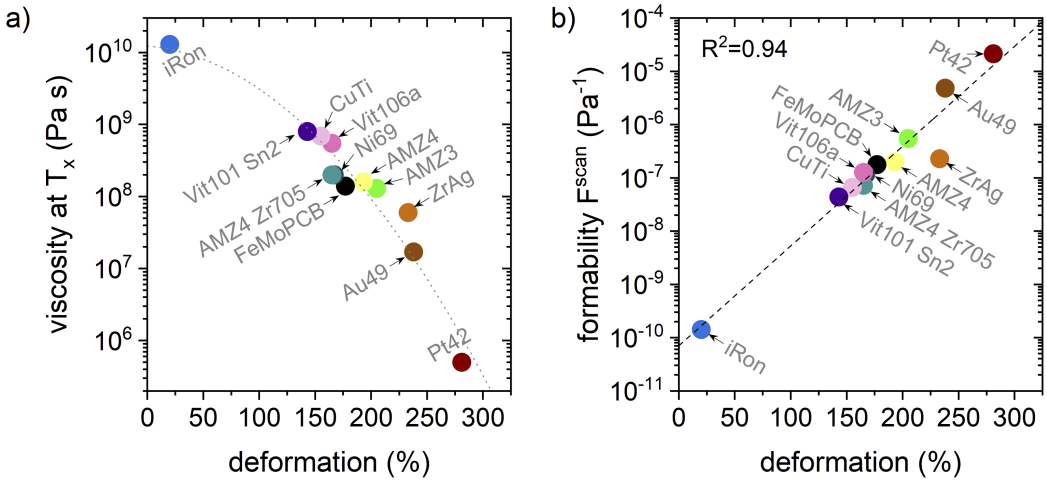

Figure 5. Correlations obtained from the TPF experiments with a constant heating rate (table 1). (a) Correlation between the viscosity at T_x, and the experimental thermoplastic deformation. The gray dotted line corresponds to a quadratic fit that is only intended to guide the eye. (b) Correlation between the formability F^{scan} according to equation (5) and the deformation. The dashed line is a linear fit to the data.

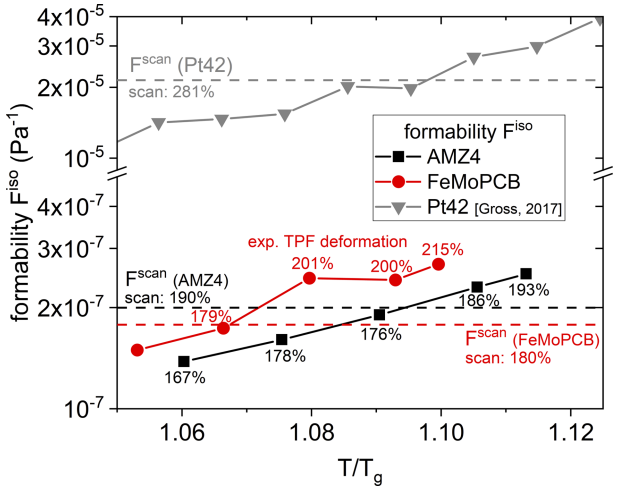

Figure 6. Isothermal formability, F^{iso}, displayed over T_g-scaled temperature. Data for AMZ4 (black), FeMoPCB (red), and Pt42 (gray) is shown. For each formability datapoint, the experimentally obtained TPF deformation is noted in %. The dashed lines indicate the values of the formability parameter for constant heating, F^{scan} and the corresponding experimental deformation is also noted.

around 200% with our experimental conditions roughly corresponds to a value of $F^{iso} = 2.5 \times 10^{-7}$ Pa^{-1}. The results also confirm the findings of Bryn Pitt *et al* that the highest formability is observed at the highest temperatures where crystallization can still be avoided [49]. Hence, the drop in viscosity at higher temperatures overcompensates the decreasing crystallization times, indicating that TPF should be performed at the upper end of the experimentally accessible temperature range.

The dashed lines in figure 6 indicate the values of the formability parameter for constant heating, F^{scan}, as previously calculated, on the same scale. For all alloys, the formability during a scan lies among the values of F^{iso}, whereas the maximum formability upon isothermal processing exceeds the formability during a scan. This is in good agreement with the measured TPF deformation values that are written next to the dashed lines indicating F^{scan}. While rather high temperatures and hence low viscosities are reached during the scan, only a short amount of pressing time is associated to this temperature region. Therefore, the overall formability during a scan stays below the values achievable during isothermal pressing.

In our experimental setup, processing temperatures that require processing times much shorter than 1 min are not feasible anymore. Such experiments were performed, but mostly resulted in the crystallization of the sample. At such high temperatures, the outer parts of the sample can already start to crystallize before the whole sample is heated homogeneously and starts to deform in the center. For TPF experiments at high temperatures, a different experimental setup becomes necessary, where the sample can be heated fast and homogeneously. In fact, Johnson *et al* demonstrated that crystallization can be beaten by millisecond heating and processing [16]. They use a rapid capacitive discharge method where the sample is heated by the ohmic heat of a millisecond current pulse and heating rates of 10^6 K s^{-1} can be achieved. Later, Kaltenboeck *et al* demonstrated the feasibility of this technique for near-net shaping of a fine precision part, when the sample can be heated to the ideal TPF processing range at viscosities below 10^4 Pa s at high temperatures [17].

Commonly, the length of the SCL region, ΔT_x, is interpreted as an indicator of the thermoplastic formability, however the deformation experiments in this work showed no direct correlation. As discussed before, the formability during a scan is mainly determined by the minimum viscosity that can be reached before crystallization occurs, $\eta(T_x)$. Consequently, in order to better understand the important influence of the other material properties on the formability during a scan, their influence on viscosity is visualized in figure 7.

Figure 7(a) shows the influence of the glass transition temperature, T_g, on the minimum viscosity. Three systems with the same ΔT_x value of 80 K and the same kinetic fragility of $D^* = 20$, are displayed over a T_g-scaled temperature axis. The alloy with the lowest T_g reaches much lower viscosity values than the alloys with higher glass transition temperatures.

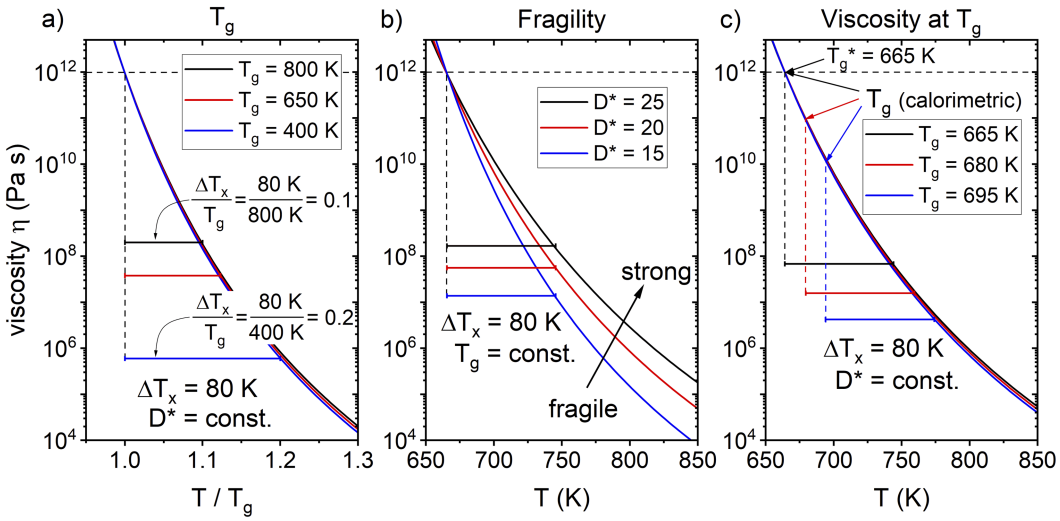

Figure 7. Influence of (a) the glass transition temperature T_g, (b) the kinetic fragility, and (c) the viscosity at T_g, on the viscosity at the onset of crystallization. A lower viscosity at the end of the SCL region (at T_x) causes a higher thermoplastic formability. For all systems, the value of ΔT_x is constant, in order to visualize the influence of the other properties on the formability.

A simple calculation is shown within the plot to visualize the effect of T_g. On the T_g-scaled axis, a lower T_g value causes the corresponding SCL region to be larger and therefore lower viscosity values are reached, given the same fragility. Hence, the sole length of the SCL region cannot account for the influence of the intrinsic temperature of the system on the formability. The T_g-scaling however, corrects for this influence which explains the good correlation of $\Delta T_x/T_g$ with the formability. Accordingly, the excellent formability of the Pt42 and Au49 alloy (compare to table 1) are based on their low T_g-values.

In figure 7(b), the influence of the kinetic fragility on the viscosity above the glass transition is visualized. Given the same T_g and the same ΔT_x, the more fragile systems with a lower D^*-value reach a much lower viscosity at the onset of crystallization and hence show a better thermoplastic formability.

Finally, the influence of the viscosity at the calorimetric glass transition temperature, T_g, is depicted in figure 7(c). In theory, a viscosity of 10^{12} Pa s is assumed at the glass transition temperature, leading to the definition of the kinetic glass transition temperature, $T_g{}^*$ [30]. Some alloys, however, show much lower viscosity values at their calorimetric glass transition temperature (measured by DSC), leading to a temperature offset of many degrees between T_g and $T_g{}^*$. In the case of the Pt42 alloy for example, T_g (=514 K) and $T_g{}^*$ (=498 K) are 16 K apart [31]. Similar offsets are observed for Au-based alloys (e.g. Au49 from table 1 with an offset of 13 K) [32] and Mg-based ones [33]. All of these alloys have in common that they possess a relatively low glass transition temperature: T_g (Pt42) = 514 K, T_g (Au49) = 396 K, and T_g (Mg-based) ≈ 420 K. These findings suggest that T_g and $T_g{}^*$ deviate relatively strong for metallic glasses with a low T_g. Similar observations were also made for molecular liquids with low T_g, where viscosity at the calorimetric glass transition is around 10^{10} Pa s [50]. Figure 7(c) shows three systems with the same values of ΔT_x, $T_g{}^*$, and D^*, where only the viscosity at T_g (calorimetric) differs. Obviously, the alloy with the lowest viscosity at T_g also shows the lowest viscosity at T_x, and hence the highest thermoplastic formability.

In the case of the Pt42 and the Au49 alloy, the large thermoplastic formability can be explained by the combination of the effects presented in figures 7(a) and (c). They both show low T_g-values and at the same time a relatively low viscosity at their calorimetric T_g. The same findings are true for the well-known Pd-based BMGs, which were not included in this study, and hence they are also expected to display a similarly high thermoplastic formability. The kinetic and thermodynamic properties of the Pd-based BMG $Pd_{43}Ni_{10}Cu_{27}P_{20}$ were previously investigated [51, 52]. This alloy shows a relatively low T_g of 584 K, an even lower $T_g{}^*$ of 568 K [52], and a large supercooled liquid region of ΔT_x = 95 K. The TPF experiments of Schroers [47], and also other works on the thermoplastic deformation of Pd-based BMGs [10, 11, 53], confirm their excellent formability.

5. Summary and conclusions

The formability of BMGs is evaluated and discussed in connection to their thermophysical properties, which is an important basis for the application of thermoplastic processing techniques for amorphous metals on the industrial scale. Formability is experimentally assessed by two different approaches, first, TPF experiments with a constant heating rate, and second, isothermal experiments. For both cases, formability is also calculated from previously measured material properties and found to perfectly coincide with the experimental deformation results. The highest formability is obtained at the highest temperatures that can be reached while still avoiding crystallization.

The TPF experiments with a constant heating rate show that the obtained deformation varies strongly between different alloys. A correlation between deformation and the two parameters $\Delta T_x/T_g$ and $S = \Delta T_x/(T_l - T_g)$, which can simply be calculated from a single calorimetric measurement, is observed.

An even stronger correlation with deformation is found for two quantities that can be obtained from a single TMA viscosity scan. First, the viscosity just before T_x, and second, the formability F^{scan}, as calculated according to equation (5). This also verifies the validity of the theoretical concept behind the formability F^{scan}, which can be calculated from the viscosity data in the temperature range between T_g and T_x.

The isothermal deformation experiments on AMZ4 and FeMoPCB demonstrate that the highest deformation is reached at the upper limit of the accessible temperature processing window, where crystallization can still be avoided. The experimental TTD diagrams for both alloys are displayed in figure 3. These results align well with the theoretical temperature-dependent formability calculated from isothermal crystallization times and viscosity values.

Acknowledgments

The authors wish to thank B Reiplinger and C Paulo for their experimental support. Furthermore, we are grateful to O Gross, A Kuball, M Frey, and N Neuber for countless lively and useful discussions.

ORCID iDs

Benedikt Bochtler https://orcid.org/0000-0003-0494-735X

References

[1] Schroers J 2010 Processing of bulk metallic glass *Adv. Mater.* **22** 1566–97
[2] Leamy H J, Wang T T and Chen H S 1972 Plastic flow and fracture of metallic glass *Metall. Trans.* **3** 699–708
[3] Patterson J P and Jones D R H 1978 Moulding of a metallic glass *Mater. Res. Bull.* **13** 583–5
[4] Peker A and Johnson W L 1993 A highly processable metallic glass: $Zr_{41.2}Ti_{13.8}Cu_{12.5}Ni_{10}Be_{22.5}$ *Appl. Phys. Lett.* **63** 2342–4
[5] Schroers J and Johnson W L 2004 Highly processable bulk metallic glass-forming alloys in the Pt–Co–Ni–Cu–P system *Appl. Phys. Lett.* **84** 3666–8
[6] Schroers J 2005 The superplastic forming of bulk metallic glasses *JOM* **57** 35–9
[7] Schroers J, Nguyen T, O'Keeffe S and Desai A 2007 Thermoplastic forming of bulk metallic glass—applications for MEMS and microstructure fabrication *Mater. Sci. Eng.* A **449** 898–902
[8] Li N, Chen W and Liu L 2016 Thermoplastic micro-forming of bulk metallic glasses: a review *JOM* **68** 1246–61
[9] Kumar G, Tang H X and Schroers J 2009 Nanomoulding with amorphous metals *Nature* **457** 868–72
[10] Chen N, Yang H A, Caron A, Chen P C, Lin Y C, Louzguine-Luzgin D V, Yao K F, Esashi M and Inoue A 2011 Glass-forming ability and thermoplastic formability of a Pd40Ni40Si4P16 glassy alloy *J. Mater. Sci.* **46** 2091–6
[11] Liu X, Chen N, Gu J-L, Yang G-N, Mussler G and Yao K-F 2015 Die imprinting of MGs: a one-step approach for large-area metallic photonic crystals *Mater. Des.* **87** 1018–21
[12] Saotome Y, Miwa S, Zhang T and Inoue A 2001 The micro-formability of Zr-based amorphous alloys in the supercooled liquid state and their application to micro-dies *J. Mater. Process. Technol.* **113** 64–9
[13] Schroers J, Pham Q, Peker A, Paton N and Curtis R V 2007 Blow molding of bulk metallic glass *Scr. Mater.* **57** 341–4
[14] Schroers J, Hodges T M, Kumar G, Raman H, Barnes A J, Pham Q and Waniuk T A 2011 Thermoplastic blow molding of metals *Mater. Today* **14** 14–9
[15] Kim Y H, Lim K R, Kim W T, Kim D H, Choi Y S and Na Y S 2019 Rapid heating blow molding of metallic glasses by infrared heating *Results Mater* **3** 100045
[16] Johnson W L, Kaltenboeck G, Demetriou M D, Schramm J P, Liu X, Samwer K, Kim C P and Hofmann D C 2011 Beating crystallization in glass-forming metals by millisecond heating and processing *Science* **332** 828–33
[17] Kaltenboeck G, Harris T, Sun K, Tran T, Chang G, Schramm J P, Demetriou M D and Johnson W L 2015 Accessing thermoplastic processing windows in metallic glasses using rapid capacitive discharge *Sci. Rep.* **4** 6441
[18] Kaltenboeck G, Demetriou M D, Roberts S and Johnson W L 2016 Shaping metallic glasses by electromagnetic pulsing *Nat. Commun.* **7** 10576
[19] Zhang W, Miao H, Li Y, Chang C, Xie G and Jia X 2017 Glass-forming ability and thermoplastic formability of ferromagnetic (Fe, Co, Ni) 75 P 10 C 10 B 5 metallic glasses *J. Alloys Compd.* **707** 57–62
[20] Song S M, Liao Y C, Li T H, Lee C K, Tsai P H, Jang J S C and Huang J C 2019 Thermoplastic deformation behavior of a Fe-based bulk metallic glass within the supercooled liquid region *J. Mater. Res. Technol.* **8** 1907–14
[21] Bera S, Sarac B, Balakin S, Ramasamy P, Stoica M, Calin M and Eckert J 2017 Micro-patterning by thermoplastic forming of Ni-free Ti-based bulk metallic glasses *Mater. Des.* **120** 204–11
[22] Shamlaye K F, Laws K J and Ferry M 2016 Supercooled liquid fusion of carbon fiber-bulk metallic glass composites with superplastic forming properties *Scr. Mater.* **111** 127–30
[23] Monfared A, Liu W and Zhang L 2017 On the adhesion between metallic glass and dies during thermoplastic forming *J. Alloys Compd.* **711** 235–42
[24] Kuball A, Bochtler B, Gross O, Pacheco V, Stolpe M, Hechler S and Busch R 2018 On the bulk glass formation in the ternary Pd-Ni-S system *Acta Mater.* **158** 13–22
[25] Kui H W, Greer A L and Turnbull D 1984 Formation of bulk metallic glass by fluxing *Appl. Phys. Lett.* **45** 615–6
[26] Bochtler B, Gross O, Gallino I and Busch R 2016 Thermo-physical characterization of the Fe67Mo6Ni3.5Cr3.5P12C5.5B2.5 bulk metallic glass forming alloy *Acta Mater.* **118** 129–39
[27] Hagy H E 1963 Experimental evaluation of beam-bending method of determining glass viscosities in the range 10^8 to 10^{15} poises *J. Am. Ceram. Soc.* **46** 93–7
[28] Bochtler B, Stolpe M, Reiplinger B and Busch R 2018 Consolidation of amorphous powder by thermoplastic forming and subsequent mechanical testing *Mater. Des.* **140** 188–95
[29] Waniuk T A A, Busch R, Masuhr A and Johnson W L L 1998 Equilibrium viscosity of the Zr41.2Ti13.8Cu12.5Ni10Be22.5 bulk metallic glass-forming liquid and viscous flow during relaxation, phase separation, and primary crystallization *Acta Mater.* **46** 5229–36
[30] Angell C A 1995 Formation of glasses from liquids and biopolymers *Science* **267** 1924–35
[31] Gross O, Bochtler B, Stolpe M, Hechler S, Hembree W, Busch R and Gallino I 2017 The kinetic fragility of Pt-P- and Ni-P-based bulk glass-forming liquids and its thermodynamic and structural signature *Acta Mater.* **132** 118–27
[32] Neuber N, Gross O, Eisenbart M, Heiss A, Klotz U E, Best J P, Polyakov M N, Michler J, Busch R and Gallino I 2019 The role of Ga addition on the thermodynamics, kinetics, and tarnishing properties of the Au-Ag-Pd-Cu-Si bulk metallic glass forming system *Acta Mater.* **165** 315–26

[33] Frey M, Busch R, Possart W and Gallino I 2018 On the thermodynamics, kinetics, and sub-T g relaxations of Mg-based bulk metallic glasses *Acta Mater.* **155** 117–27
[34] Schroers J, Lohwongwatana B, Johnson W L and Peker A 2005 Gold based bulk metallic glass *Appl. Phys. Lett.* **87** 94–7
[35] Gallino I, Cangialosi D, Evenson Z, Schmitt L, Hechler S, Stolpe M and Ruta B 2018 Hierarchical aging pathways and reversible fragile-to-strong transition upon annealing of a metallic glass former *Acta Mater.* **144** 400–10
[36] Zhang Q, Zhang W and Inoue A 2006 New Cu–Zr-based bulk metallic glasses with large diameters of up to 1.5cm *Scr. Mater.* **55** 711–3
[37] Inoue A, Zhang T and Masumoto T 1992 The structural relaxation and glass transition of La-Al-Ni and Zr-Al-Cu amorphous alloys with a significant supercooled liquid region *J. Non-Cryst. Solids* **150** 396–400
[38] Wang D, Tan H and Li Y 2005 Multiple maxima of GFA in three adjacent eutectics in Zr–Cu–Al alloy system – A metallographic way to pinpoint the best glass forming alloys *Acta Mater.* **53** 2969–79
[39] Zhang W, Jia X, Li Y and Fang C 2014 Effects of Mo addition on thermal stability and magnetic properties of a ferromagnetic $Fe_{75}P_{10}C_{10}B_5$ metallic glass *J. Appl. Phys.* **115** 17A768
[40] Na J H, Demetriou M D, Floyd M, Hoff A, Garrett G R and Johnson W L 2014 Compositional landscape for glass formation in metal alloys *Proc. Natl Acad. Sci. USA* **111** 9031–6
[41] Heinrich J, Busch R and Nonnenmacher B 2012 Processing of a bulk metallic glass forming alloy based on industrial grade Zr *Intermetallics* **25** 1–4
[42] Hembree W 2015 High temperature rheology of Zr-based bulk metallic glass forming liquids *Dissertation* Saarland University
[43] Hays C C, Schroers J, Geyer U, Bossuyt S, Stein N and Johnson W L 2000 Glass forming ability in the Zr-Nb-Ni-Cu-Al bulk metallic glasses *J. Metastable Nanocryst. Mater.* **8** 103–8
[44] Hays C C, Schroers J, Johnson W L, Rathz T J, Hyers R W, Rogers J R and Robinson M B 2001 Vitrification and determination of the crystallization time scales of the bulk-metallic-glass-forming liquid $Zr_{58.5}Nb_{2.8}Cu_{15.6}Ni_{12.8}Al_{10.3}$ *Appl. Phys. Lett.* **79** 1605–7
[45] Park E S, Lim H K, Kim W T and Kim D H 2002 The effect of Sn addition on the glass-forming ability of Cu–Ti–Zr–Ni–Si metallic glass alloys *J. Non-Cryst. Solids* **298** 15–22
[46] Garrett G R, Demetriou M D, Chen J and Johnson W L 2012 Effect of microalloying on the toughness of metallic glasses *Appl. Phys. Lett.* **101** 241913
[47] Schroers J 2008 On the formability of bulk metallic glass in its supercooled liquid state *Acta Mater.* **56** 471–8
[48] Gross O, Riegler S S, Stolpe M, Bochtler B, Kuball A, Hechler S, Busch R and Gallino I 2017 On the high glass-forming ability of Pt-Cu-Ni/Co-P-based liquids *Acta Mater.* **141** 109–19
[49] Bryn Pitt E, Kumar G and Schroers J 2011 Temperature dependence of the thermoplastic formability in bulk metallic glasses *J. Appl. Phys.* **110** 043518
[50] Angell C A 2004 *Glass Transition Encyclopedia of Materials: Science and Technology* (Amsterdam: Elsevier) pp 1–11
[51] Fan G J, Fecht H-J and Lavernia E J 2004 Viscous flow of the Pd43Ni10Cu27P20 bulk metallic glass-forming liquid *Appl. Phys. Lett.* **84** 487–9
[52] Gallino I, Schroers J and Busch R 2010 Kinetic and thermodynamic studies of the fragility of bulk metallic glass forming liquids *J. Appl. Phys.* **108** 063501
[53] Saotome Y, Itoh K, Zhang T and Inoue A 2001 Superplastic nanoforming of Pd-based amorphous alloy *Scr. Mater.* **44** 1541–5